Feasibility of In Vivo Measurement of Carotid Wall Shear Rate Using Spiral Fourier Velocity Encoded MRI

Joao L. A. Carvalho,[1,2]* Jon-Fredrik Nielsen,[1,3] and Krishna S. Nayak[1]

Arterial wall shear stress is widely believed to influence the formation and growth of atherosclerotic plaque; however, there is currently no gold standard for its in vivo measurement. The use of phase contrast MRI has proved to be challenging due to partial-volume effects and inadequate signal-to-noise ratio at the high spatial resolutions that are required. This work evaluates the use of spiral Fourier velocity encoded MRI as a rapid method for assessing wall shear rate in the carotid arteries. Wall shear rate is calculated from velocity histograms in voxels spanning the blood/vessel wall interface, using a method developed by Frayne and Rutt (Magn Reson Med 1995;34:378–387). This study (i) demonstrates the accuracy of the velocity histograms measured by spiral Fourier velocity encoding in a pulsatile carotid flow phantom compared with high-resolution phase contrast, (ii) demonstrates the accuracy of Fourier velocity encoding–based shear rate measurements in a numerical phantom designed using a computational fluid dynamics simulation of carotid flow, and (iii) demonstrates in vivo measurement of regional wall shear rate and oscillatory shear index in the carotid arteries of healthy volunteers at 3 T. Magn Reson Med 63:1537–1547, 2010. © 2010 Wiley-Liss, Inc.

Key words: wall shear stress; oscillatory shear index; carotid artery disease; spiral Fourier velocity encoding; magnetic resonance imaging

Atherosclerosis affects over 18 million Americans. The associated formation, growth, and rupture of intraarterial plaque represent the fundamental process leading to myocardial infarction and thrombotic stroke. Arterial wall shear stress (WSS)—the drag force acting on the endothelium as a result of blood flow—is widely believed to influence the formation and growth of atherosclerotic plaque and may have prognostic value. WSS can be estimated as the product of wall shear rate (WSR) and blood viscosity (μ), where WSR is the radial gradient of blood flow velocity (dv/dr) at the vessel wall. Low WSS (1,2) and highly oscillatory WSS (3) have been linked to the formation and growth of atherosclerotic plaques, and this link has been validated in vitro (4). High WSS has also been hypothesized as a factor responsible for the topography of atherosclerotic lesions (5). Serial and noninvasive WSS measurement would be of value to the in vivo testing of these hypotheses and to better our understanding of the causal relationships between hemodynamics and the process of atherosclerotic plaque formation, growth, and rupture.

Direct methods for measuring WSS are highly invasive and/or can only be used in conjunction with in vitro models (6–8). Indirect methods for measuring WSS are based on extrapolation of the measured axial velocity profile near the vessel wall (9), which can be measured by either ultrasound (10,11) or MRI (11–16). The accuracy of such methods is limited by data quality and the spatial resolution of the velocity estimates. Particularly, phase contrast (PC) MRI suffers from partial-volume effects (17) and inadequate signal-to-noise ratio (SNR) at high spatial resolutions (Fig. 1). PC is not currently capable of providing accurate absolute measurements of WSS (18) and has been shown to underestimate blood flow velocities in the carotid bifurcation by 31–39% (19). An alternative approach for estimating WSS is to reconstruct a complex flow field via computational fluid dynamics (CFD) simulation, using vascular geometries and input/output functions derived from noninvasive imaging data (20–22). This approach is computationally intense and may be sensitive to many assumptions and simplifications that are frequently made about the properties of blood and endothelium. CFD is also limited in modeling wall compliance and is sensitive to boundary conditions (11).

In 1995, Frayne and Rutt (23) proposed a novel method for noninvasively estimating wall shear rate using Fourier velocity encoded (FVE) (24) MRI with a two-dimensional Fourier transform (2DFT) trajectory. FVE provides intrinsically higher SNR than PC and does not suffer from partial-volume effects. The Frayne method involves using the distribution of velocities measured within voxels spanning the blood/vessel wall interface as a basis for reconstructing intravoxel velocity profiles. This approach provides effective spatial resolution much finer than the voxel size and is able to determine the position of the wall-blood interface within the voxel with high accuracy. Because of the prohibitively long scan times associated with 2DFT FVE, the Frayne method has only been applied in vitro.

In this work, we evaluate the use of spiral FVE (25) with Frayne's reconstruction for estimating carotid WSR in clinically feasible scan times. We first use a signal model to compare spiral FVE with high-resolution 2DFT PC and determine the accuracy of measured velocity distributions in a pulsatile carotid flow phantom. We then compare WSR measurements from simulated spiral FVE data with those

[1]Magnetic Resonance Engineering Laboratory, Ming Hsieh Department of Electrical Engineering, University of Southern California, Los Angeles, California, USA.

[2]Digital Signal Processing Group, Department of Electrical Engineering, University of Brasília, Brasília-DF, Brazil.

[3]Functional MRI Laboratory, Department of Biomedical Engineering, University of Michigan, Ann Arbor, Michigan, USA.

Additional Supporting Information may be found in the online version of this article.

Presented at the SCMR 2008 meeting (abstract #2134), the ISMRM 2008 meeting (abstract #908), the CBEB 2008 meeting (paper #974, in Portuguese), and the ISMRM 2009 meeting (abstract #326). The CBEB paper was awarded first place by the Brazilian Society of Biomedical Engineering in its 2008 Young Investigator Awards competition.

Grant sponsor: American Heart Association; Grant number: 0435249N.

*Correspondence to: João Luiz Azevedo de Carvalho, Ph.D., Departamento de Engenharia Elétrica, Campus Universitário Darcy Ribeiro, Caixa Postal 4386, Brasília-DF, Brazil 70919-970. E-mail: joaoluiz@gmail.com

Received 24 March 2009; revised 5 November 2009; accepted 16 November 2009.

DOI 10.1002/mrm.22325
Published online in Wiley InterScience (www.interscience.wiley.com).

from a matched CFD simulation to verify the appropriateness of the Frayne method. Finally, we demonstrate the feasibility of rapid in vivo carotid WSR measurement in healthy volunteers at 3 T.

MATERIALS AND METHODS

Experimental Setup

In vitro and in vivo MRI experiments were performed on a 3-T Signa Excite HD system (GE Healthcare, Waukesha, WI), with gradients capable of 40 mT/m amplitude and 150 T/m/sec slew rate and a receiver with sampling interval of 4 μs. Pulse sequence designs were optimized for this hardware configuration. In all experiments, the body coil was used for radiofrequency transmission. A 5-inch surface coil was used for signal reception during in vitro studies. During in vivo studies, a four-channel carotid artery coil (Pathway MRI, Inc., Seattle, WA) was used for signal reception, and only data from the two elements corresponding to the left-hand side were used for reconstruction. The institutional review board of the University of Southern California approved the imaging protocols. Subjects were screened for MRI risk factors and provided informed consent in accordance with institutional policy.

Determining the Accuracy of Spiral FVE Measurements

First, an in vitro comparison of velocity distributions measured with spiral FVE with those derived from high-resolution 2DFT PC—the current MR gold standard—was performed. A signal model that incorporates spiral FVE k-space truncation effects was used to generate simulated FVE data based on high-resolution 2DFT PC data.

FVE resolves the spectrum of velocities $s(v)$ within each voxel by Fourier encoding along at least one velocity axis (24). In this work, velocity (v) is encoded only along the through-plane axis (z), and the data are spatially resolved along two in-plane axes (x, y). The FVE signal measured at each cardiac phase is a three-dimensional function: $s(x, y, v)$.

2DFT PC provides two two-dimensional functions, $m(x, y)$ and $v_o(x, y)$, the magnitude and velocity maps, respectively. If these maps are measured with sufficiently high spatial resolution and flow is laminar, one can assume that each voxel contains only one velocity, and therefore the spatial-velocity distribution associated with the object is approximately:

$$s(x, y, v) = m(x, y) \times \delta(v - v_o(x, y)), \quad [1]$$

where $\delta(v)$ is the Dirac delta function.

Spiral FVE acquisitions follow a stack-of-spirals pattern in k_x, k_y, k_v space (the k-space associated with the $s(x, y, v)$ distribution) (25). Consequently, k-space data are truncated to a cylinder, i.e., a circle along k_x, k_y (with diameter $1/\Delta r$), and a rectangle along k_v (with width $1/\Delta v$), where Δr and Δv are the prescribed spatial and velocity resolutions, respectively. The associated object domain spatial-velocity blurring can be modeled as a convolution of the true object distribution, $s(x, y, v)$, with $\mathrm{jinc}(\sqrt{x^2 + y^2}/\Delta r)$ and $\mathrm{sinc}(v/\Delta v)$, resulting in:

$$\begin{aligned}\hat{s}(x, y, v) &= [m(x, y) \times \delta(v - v_o(x, y))] * \mathrm{sinc}\left(\frac{v}{\Delta v}\right) * \mathrm{jinc}\left(\frac{\sqrt{x^2 + y^2}}{\Delta r}\right) \\ &= \left[m(x, y) \times \mathrm{sinc}\left(\frac{v - v_o(x, y)}{\Delta v}\right)\right] * \mathrm{jinc}\left(\frac{\sqrt{x^2 + y^2}}{\Delta r}\right),\end{aligned} \quad [2]$$

where $\hat{s}(x, y, v)$ is the measured object distribution and $*$ denotes convolution. In 2DFT FVE, the spatial blurring function would be $\mathrm{sinc}(x/\Delta x) \times \mathrm{sinc}(y/\Delta y)$, where Δx and Δy are the spatial resolutions along the x and y axes, respectively, resulting in:

$$\hat{s}(x, y, v) = \left[m(x, y) \times \mathrm{sinc}\left(\frac{v - v_o(x, y)}{\Delta v}\right)\right] * \left[\mathrm{sinc}\left(\frac{x}{\Delta x}\right) \times \mathrm{sinc}\left(\frac{y}{\Delta y}\right)\right]. \quad [3]$$

Experiments were performed using a pulsatile carotid flow phantom (Phantoms by Design, Inc., Bothell, WA). A slice perpendicular to the carotid bifurcation was prescribed, and through-plane velocities were measured. A cine gradient-echo 2DFT PC sequence with high spatial resolution and high SNR (0.33 mm resolution, 10 averages, 80 cm/sec Venc) was used as a reference. CINE spiral FVE data with $\Delta r = 3$ mm and $\Delta v = 10$ cm/sec were obtained from the same scan plane. Both acquisitions were prospectively gated and used the same pulse repetition time (11.6 ms), flip angle (30°), slice profile (3 mm), temporal resolution (23.2 ms), and prescan settings. The total scan time was 40 min for PC and 12 sec for FVE.

A simulated spiral FVE dataset was computed from the PC magnitude and velocity maps, using the convolution model described in Eq. 2. The PC-derived and FVE-measured data were registered by taking one magnitude image $m(x, y)$ from each dataset and then using the phase difference in their Fourier transforms $M(k_x, k_y)$ to estimate the spatial shift between the images. Amplitude scaling was performed by normalizing the ℓ_2-norm of each FVE dataset. The difference between PC-derived and FVE-measured time-velocity distributions was calculated for select voxels, and the associated signal-to-error ratios were computed. This was used as a quantitative assessment of spiral FVE's accuracy.

Determining the Accuracy of WSR Measurements

The proposed method for WSR estimation consists of using spiral FVE to measure the distribution of velocities near the vessel wall and then using the Frayne method to estimate the corresponding shear rate. No gold standard currently exists for assessing carotid WSR. Thus, a simulation was used for investigating the feasibility of the proposed approach. The convolution model described in Eq. 2 was used to produce simulated spiral FVE distributions from a high-resolution velocity map, which was obtained using CFD simulation of carotid flow. Then, the Frayne method was used to measure shear rate values from the simulated spiral FVE distributions, as described below. Finally, the FVE shear rates were compared with the

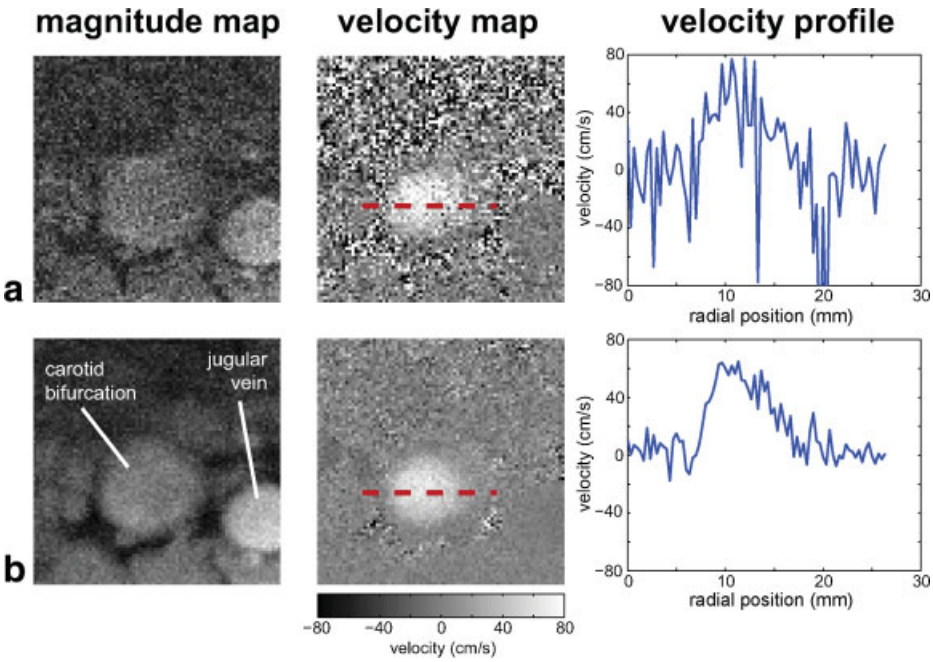

FIG. 1. Illustration of in vivo high-resolution 2DFT PC MRI, obtained at the carotid bifurcation of a healthy volunteer at peak flow: **(a)** single acquisition; **(b)** 10 signal averages. High spatial resolution is typically associated with low SNR **(a)**. Averaging multiple acquisitions improves SNR **(b)** but also increases the total scan time and may cause loss of effective resolution due to subject motion. Scan parameters: $0.33 \times 0.33 \times 3$ mm^3 spatial resolution, 37-ms temporal resolution, 30° flip angle, 80 cm/sec Venc, 2-min scan (120 heartbeats) per acquisition. [Color figure can be viewed in the online issue, which is available at www.interscience.wiley.com.]

true gradient values, measured on the high-resolution CFD velocity map.

The Frayne method for FVE-based WSR estimation (23) involves obtaining the velocity distribution for a voxel spanning the blood/vessel wall interface and then using this distribution to reconstruct the velocity profile across the voxel, with subvoxel spatial resolution. Assuming that signal intensity is spatially and velocity invariant, the sum of the signals from all velocities within a voxel is proportional to the total volume of material within the voxel. Furthermore, two assumptions can be made about the shape of the velocity profile: (i) the fluid velocity at the vessel wall is approximately zero, and (ii) the velocity profile within a voxel is monotonically increasing or decreasing. Using these assumptions, a stepwise discrete approximation $\tilde{v}(r)$ to the true velocity profile across a voxel can be obtained from its velocity distribution $s(v)$ by inverting the discrete function $r(v)$, which is constructed as follows:

$$r(v_i) = r(v_{i-1}) + \Delta r \cdot h(v_i), \quad \text{where } h(v_i) = \frac{|s(v_i)|}{\sum_v |s(v)|}. \quad [4]$$

Note that for each velocity bin v_i, the intravoxel position r is incremented by a fraction of the total radial extent of the voxel (Δr). This fraction is proportional to $h(v_i)$, which is the volume fraction of the voxel that has velocity $v = v_i$. The volume fractions are calculated by normalizing the velocity distribution. This process is demonstrated graphically in Fig. 2. Spatial variations in signal intensity due to radiofrequency saturation (i.e., inflow enhancement) and due to differences in ^{1}H density and relaxation properties between vessel wall tissue and blood may be compensated by adjusting $s(v)$ accordingly, prior to calculating $h(v)$ (23).

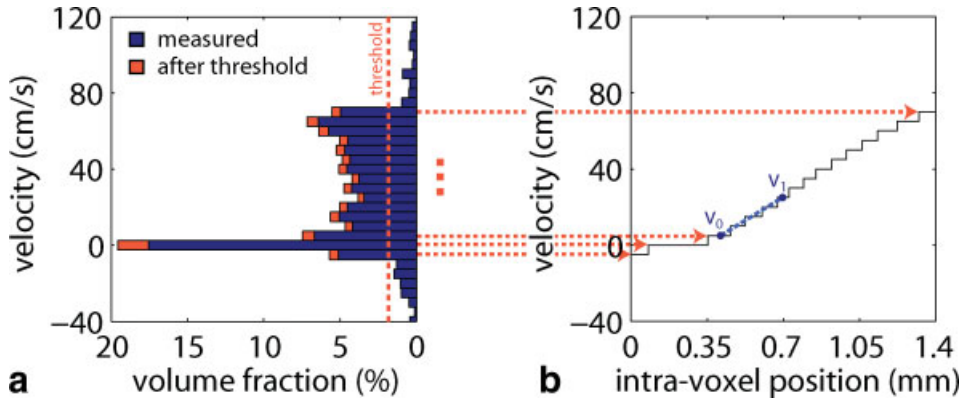

FIG. 2. Graphical illustration of the Frayne method (23). WSR is estimated from FVE velocity distributions in voxels spanning the blood/vessel wall interface. First, a threshold is applied to the velocity histogram to reduce noise sensitivity **(a)**. Then, the volume fraction within each velocity bin is converted into a radial position across the voxel, using Eq. 4. Finally, the velocity gradient is estimated from the reconstructed velocity profile **(b)**, within a small velocity interval $[v_0, v_1]$. [Color figure can be viewed in the online issue, which is available at www.interscience.wiley.com.]

In order to reduce the effects of ringing and noise rectification due to the magnitude operation in Eq. 4, a threshold is applied to $s(v)$ before normalization (Fig. 2a). The appropriate threshold level must be determined by analyzing the signal intensities in the velocity distribution for a range of velocities outside the range of expected blood flow velocities. It is assumed that signal outside this expected range is exclusively due to rectified noise (23). In our implementation, only components that are below the specified threshold *and* outside this expected range of velocities are set to zero.

The WSR can be estimated by prescribing a velocity interval $[v_0,v_1]$ and then fitting a first-order polynomial to the points of $\tilde{v}(r)$ within this interval (Fig. 2b). Ideally, $v_0 = 0$ and $v_1 = \Delta v$ because we wish to estimate the velocity derivative at the blood-wall interface. The SNR of shear rate estimates will increase as this velocity interval becomes larger because of averaging across multiple velocity steps. However, as the interval becomes larger, the shear rate is averaged over a larger distance within the voxel and may deviate from the true local shear at the wall (23). Therefore, it is important to prescribe a reasonable $[v_0,v_1]$ interval. In our implementation, $v_0 = \Delta v$ and $v_1 \approx 30$ cm/sec are used for an initial assessment, and then the interval is manually adjusted for selected voxels of interest. The same voxel-based approach is used with respect to the noise threshold discussed above, with a fixed threshold value being used for the initial assessment. A negative $[v_0,v_1]$ interval—e.g., $v_0 = -5$ cm/sec and $v_1 = -15$ cm/sec—is used when large volume fractions are measured on negative velocities, i.e., when there are large $h(v)$ values for $v < 0$. This allows measuring negative WSR values.

CFD simulations were performed using Fluent (Ansys, Inc., Lebanon, NH). A carotid bifurcation geometry was designed, and the flow simulation was performed under steady-state conditions with a maximum center-line velocity of 120 cm/sec, and with a mean Reynolds number of 289 (26). An axial map of through-plane velocities was obtained and interpolated onto a Cartesian grid. The corresponding WSR map was calculated using first-order two-dimensional polynomial-weighted least-squares fit and was used as ground truth.

Simulated spiral FVE data were obtained from the CFD velocity map, using Eq. 2. Signal intensities were assumed to be uniform throughout the object, i.e., $m(x,y) = 1$. The simulated spatial and velocity resolutions were $\Delta r = 1$ mm and $\Delta v = 12.5$ cm/sec, over a ± 200 cm/sec velocity field of view (32 velocity encode levels).

The Frayne method was then used to estimate WSR. The noise threshold level was set to 2.5% of the ℓ_1-norm of the velocity distribution. WSR values were estimated for different choices of $[v_0,v_1]$ intervals in order to evaluate the method's sensitivity to the interval's length and center. The results were quantitatively compared with the WSR map measured directly from the CFD velocity map.

Demonstrating the Feasibility of In Vivo WSR Measurement

Next, the in vivo measurement of carotid WSR using CINE spiral FVE acquisitions with Frayne's reconstruction was demonstrated. Three healthy subjects were studied. One of the subjects was studied twice, with a 2-week interval, to investigate repeatability. For each volunteer, five 5 mm contiguous slices (2.5-cm coverage) were prescribed perpendicular to the left carotid bifurcation. Each slice was imaged independently (separate acquisitions). Localized gradient shimming was performed, and acquisitions were prospectively electrocardiogram (ECG) gated. Several cardiac phases were acquired, spanning the systolic portion of the cardiac cycle. A time-bandwidth product 2 radiofrequency pulse was used for excitation, and the flip angle was 30°. Only through-plane velocities were measured, using 32 k_v encoding steps over a 160 cm/sec velocity field of view (5 cm/sec resolution). The velocity field of view was shifted from the -80 to 80 cm/sec range to the -40 to 120 cm/sec range during reconstruction in order to avoid aliasing and maximize field of view usage. Negative velocities are encoded in order to assess negative WSR values and also to accommodate leakage and ringing due to k_v truncation (i.e., finite velocity resolution). Spatial encoding was performed using eight 4-ms variable-density spiral interleaves ($16 \sim 4$ cm field of view, 1.4 mm resolution). The temporal resolution was 24 ms (12-ms pulse repetition time, two views per beat). Scan time was 128 heartbeats per slice, i.e., approximately 2 min per slice.

Reconstruction was performed in Matlab (The MathWorks, Inc., Natick, MA), and WSR estimates for each voxel in each slice and cardiac phase were obtained using the Frayne method. Spatial variations in signal intensity due to inflow enhancement and density/relaxation differences between vessel wall and blood were compensated as proposed by Frayne and Rutt (23). The noise threshold level was set to 2.5% of the ℓ_1-norm of the velocity distribution, and the shear rates were estimated within the $[v_0,v_1]$ interval of 5–25 cm/sec. Only cardiac phases within ± 72 ms of peak flow velocity were reconstructed.

Estimating Oscillatory Shear Index

Finally, the estimation of oscillatory shear index (OSI) with the proposed method was demonstrated both in vitro and in vivo. The OSI is important for the evaluation of shear stress imposed by pulsatile flow. This index describes the shear stress acting in directions other than the direction of the temporal mean shear stress vector (3,27). In this work, OSI was calculated as defined by He and Ku (27), and assuming spatially and temporally invariant blood viscosity.

Measuring negative WSR with the proposed method requires voxels to be small enough to contain only reverse flow. Voxels containing both forward and reverse flow would violate the assumption of a monotonically increasing or decreasing velocity profile within the voxel. Under sufficient spatial resolution, negative WSR may be measured simply by using a negative $[v_0,v_1]$ interval.

As a proof of concept, a simulation was used for investigating the feasibility of measuring negative WSR with the proposed method. For this experiment, we used data from the previously discussed in vitro study. It would not be possible to obtain reliable shear rate estimates directly from the measured FVE data because the vessel wall and other static materials in the phantom do not generate any MR signal (see Fig. 3a, discussed later). Thus, simulated spiral FVE data were derived from the velocity maps measured with high-resolution 2DFT PC, using Eq. 2. Signal intensities were assumed to be uniform throughout the object, i.e., $m(x,y) = 1$. The simulated spatial and velocity resolutions were $\Delta r = 1$ mm and $\Delta v = 5$ cm/sec, over a ± 80 cm/sec velocity field of view (32 velocity encode levels).

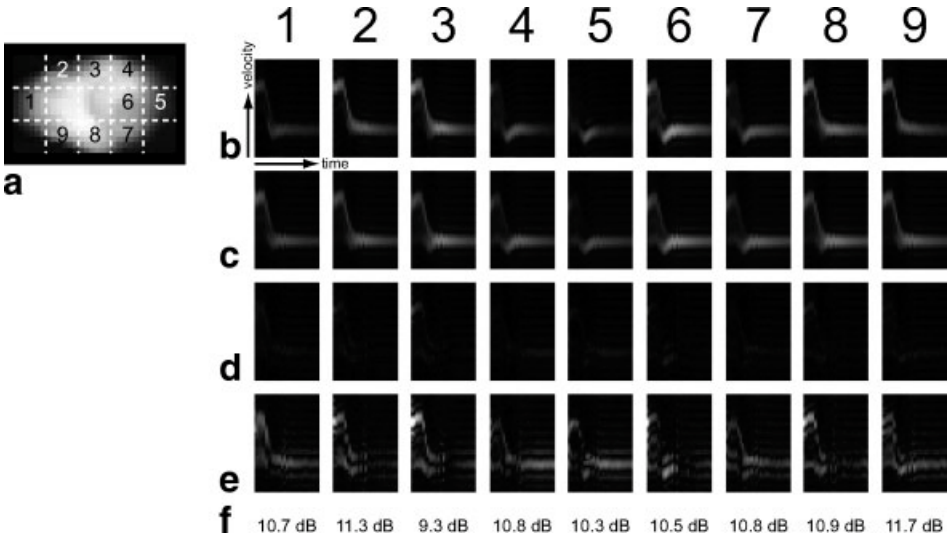

FIG. 3. In vitro evaluation of the accuracy of spiral FVE velocity histograms. Results are shown for nine representative voxels, selected around the circumference of the vessel wall of the pulsatile carotid flow phantom's bifurcation **(a)**. For each voxel, is shown **(b)** time-velocity distribution derived from high-resolution 2DFT PC; **(c)** time-velocity distribution measured with spiral FVE, **(d)** absolute difference between spiral FVE and 2DFT PC-derived histograms, **(e)** 4-fold magnification of the difference, and **(f)** signal-to-error ratio.

A voxel near the wall on the side of the phantom's external carotid artery was selected. In this voxel, an alternation between forward and reverse flow was observed. For each temporal frame, the intravoxel velocity profile was estimated from the simulated FVE velocity distribution using Eq. 4. The estimated profile was qualitatively compared with the true profile from the PC velocity map. This was performed only for select cardiac phases, corresponding to instants of positive and negative shear stress, respectively. Then, the WSR was estimated for each temporal frame in the systolic portion of the flow cycle, and the corresponding OSI was calculated. The noise threshold level and the $[v_0,v_1]$ interval were manually defined for each temporal frame.

In vivo OSI estimation was demonstrated using data from the previously discussed studies. The data from the three subjects were examined, and the subject presenting the most significant postsystolic retrograde flow was selected for this evaluation. Only data from the central slice (carotid bifurcation) were used. Eight voxels around the circumference of the vessel wall were selected. The WSR was estimated for each voxel and for each temporal frame in the systolic portion of the cardiac cycle, using the Frayne method. The noise threshold level and the $[v_0,v_1]$ interval were manually prescribed. Then, the OSI for each voxel was calculated.

RESULTS

Accuracy of Spiral FVE Measurements

Figure 3 shows measured and PC-derived time-velocity FVE distributions from nine representative voxels, selected around the circumference of the vessel wall of the pulsatile carotid flow phantom's bifurcation. The signal-to-error ratio between measured and PC-derived time-velocity distributions was measured to be within 9.3–11.7 dB. Imperfect registration between the datasets, combined with spatial blurring due to off-resonance in the measured spiral

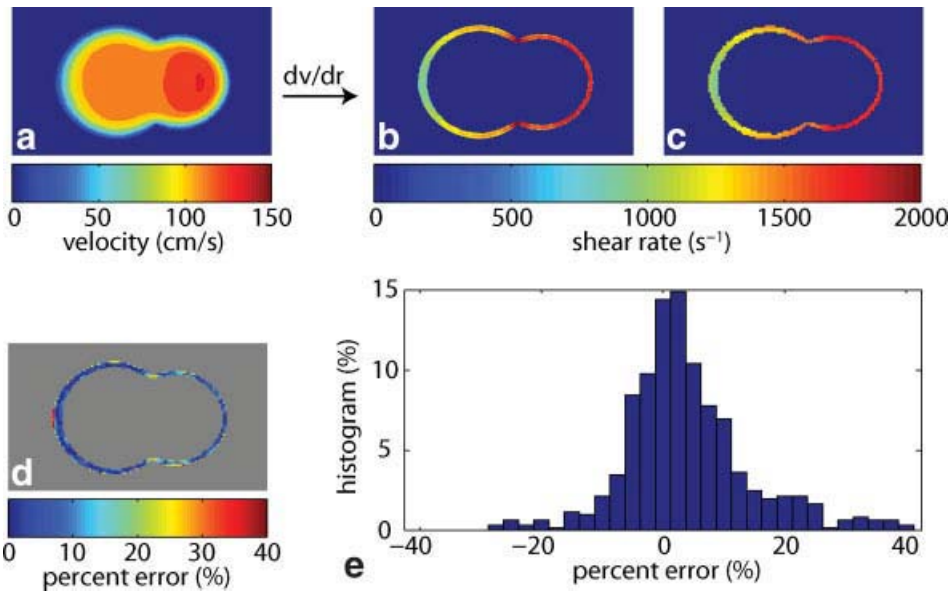

FIG. 4. Quantitative evaluation of FVE-based WSR estimation. Simulated spiral FVE data were derived from a CFD velocity map **(a)**. Within a region of interest, defined near the wall-lumen interface, the estimated shear rates **(c)** agree well with the true values **(b)**. The spiral FVE/Frayne method was able to estimate the shear rate with less than 15% error for 84% of the voxels within the region of interest **(d,e)**.

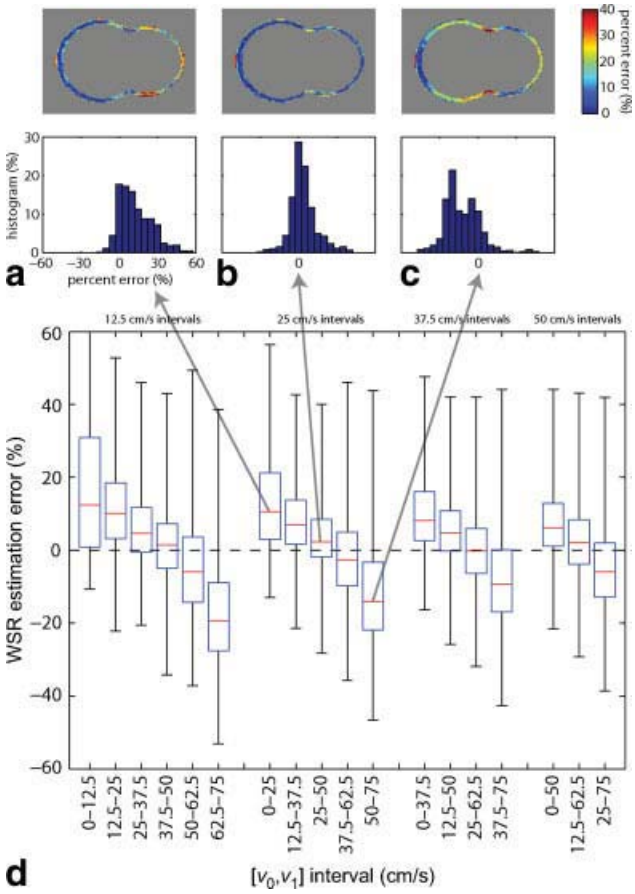

FIG. 5. Evaluation of the method's sensitivity to the choice of [v_0,v_1] interval, in a simulation using spiral FVE distributions derived from a CFD velocity map. The box-and-whisker diagrams **(d)** show the median WSR estimation percent age error (red lines), as well as the lower and upper quartile values (blue boxes) and the dynamic range (whiskers) for different choices of [v_0,v_1] interval. The results are grouped based on the length of the intervals. Intervals covering only low velocities tend to cause overestimation of WSR values, while intervals covering only high velocities tend to cause underestimation. Error maps and histograms are shown for the following [v_0,v_1] intervals: **(a)** 0–25 cm/sec; **(b)** 25–50 cm/sec; **(c)** 50–75 cm/sec.

FVE data, may have contributed to this moderate signal-to-error ratio. Nevertheless, the two datasets show good visual agreement, and no significant spatial variation was observed in terms of accuracy.

Accuracy of WSR Estimation

Figure 4 presents the results of the WSR simulation for the [v_0,v_1] interval of 25–50 cm/sec. Within a region of interest, defined around the wall-lumen interface, the proposed method was able to estimate WSR with $\leq$10% error for 73% of the voxels, $\leq$20% error for 90% of the voxels, and $\leq$30% error for 97% of the voxels. The results show an overestimation in WSR of 3.8% $\pm$ 10.4% (Fig. 4e). The median error was 2.3%. The error distribution failed normality tests. The estimation precision was reasonably uniform around the circumference of the vessel (Fig. 4d).

Figure 5 presents the results of the evaluation of the method's sensitivity to the choice of [v_0,v_1] interval. The results show that intervals covering only low velocities tend to cause overestimation of WSR values, while intervals covering only high velocities tend to cause underestimation. The results also suggest that the interval's center has a much more significant impact on WSR estimation accuracy than the interval's length.

In Vivo WSR Measurement

Figures 6 and 7 show two representative sets of in vivo results. The WSR values are shown for manually segmented regions of interest. Figure 6 illustrates the variation in WSR along all three spatial dimensions near the carotid bifurcation of subject #1. These results correspond to the cardiac phase with the highest peak velocity. Figure 7 illustrates the temporal variation of pulsatile WSR in the common carotid artery of subject #2. The results show a circumferential variation in WSR around the wall of the common carotid artery. Markl et al. (15) recently observed a similar variation using a PC-based approach.

Note that, in regions of low WSR, the region of interest was not drawn exactly at the interface between the lumen and vessel wall (center slice in Fig. 6, and temporal frames at 120 ms and 144 ms in Fig. 7). WSR overestimation is observed in voxels that contain little signal within the prescribed [v_0,v_1] interval (5–25 cm/sec). This is the case for voxels located exactly at the lumen/wall interface in regions of low WSR. In those voxels, most of the signal components are within the 0–5 cm/sec range, while the shear rate is being measured on the 5–25 cm/sec interval. Thus, we selected adjacent voxels slightly farther from the wall but still placed within the viscous sublayer. Alternatively, a different [v_0,v_1] interval may be used in those regions (see Fig. 5).

Figure 8 presents the results of the repeatability evaluation studies (subject #3). Considerable visual similarity was

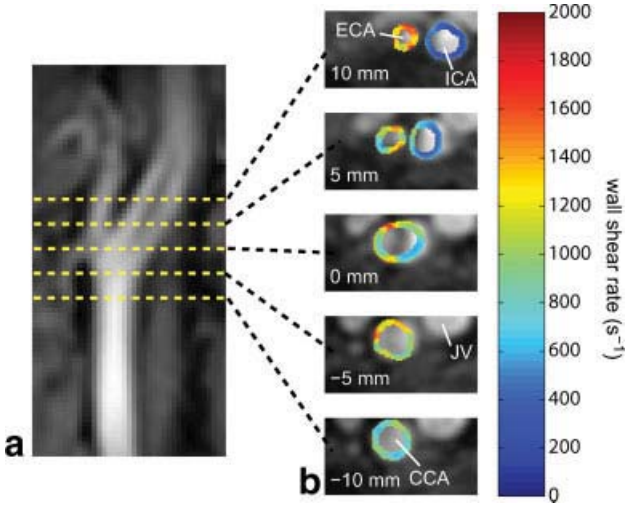

FIG. 6. Carotid WSR measured across the carotid bifurcation of subject #1: **(a)** slice prescription; **(b)** spiral FVE WSR measurements. Results correspond to the cardiac phase with the highest peak velocity (96 ms after the ECG trigger). The common (CCA), external (ECA), and internal (ICA) carotid arteries and the jugular vein (JV) are indicated.

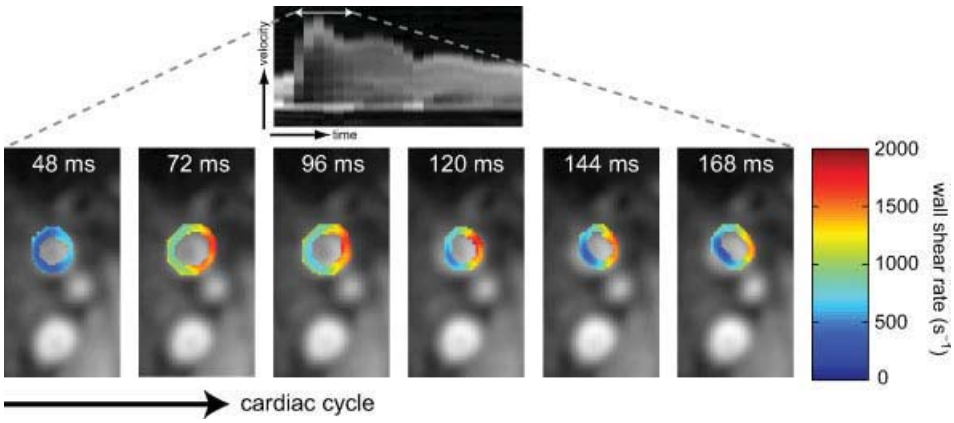

FIG. 7. Temporal variation of pulsatile WSR measured in the common carotid artery of subject #2. Results correspond to the cardiac phases acquired 48–168 ms after the ECG trigger and to a slice prescribed 10 mm below the bifurcation. [Color figure can be viewed in the online issue, which is available at www.interscience.wiley.com.]

observed between the two studies. Specifically, regions of low and high WSR match reasonably well (arrows). Nevertheless, some differences between the WSR estimates are observed. These may be due in part to differences in slice prescription and in hemodynamic conditions. The latter may have played an important role as the volunteer's heart rate was 64 beats/min during the first study, and 74 beats/min during the second study.

OSI Estimation

Figure 9 presents the results of the simulation experiment designed as a proof of concept for measurement of negative WSR and estimation of OSI. The results show that the proposed method is capable of distinguishing between positive (Fig. 9e) and negative (Fig. 9h) shear rates. The velocity profiles estimated with the proposed method show reasonable agreement with the original profiles and achieve effective spatial resolution much finer than that of high-resolution PC. We believe that better agreement would be observed if the PC velocity map had higher spatial resolution and higher SNR. WSR values measured during the systolic portion of the flow cycle are shown in Fig. 9b. As expected, segments of positive and negative WSR are associated with segments of forward and reverse flow, respectively (Fig. 9a). The OSI for the voxel of interest was estimated to be 0.19.

Figure 10 presents a demonstration of in vivo OSI estimation, using the proposed method. Results are shown for eight representative voxels, selected around the circumference of the wall of the carotid bifurcation of subject #3. Measured velocity distributions, WSRs, and OSI values, corresponding to the systolic portion of the cardiac cycle, are shown for each voxel. High OSI values were observed at the wall corresponding to the carotid bulb. Nonzero OSI was also observed at the opposite wall. These findings are in agreement with PC-based OSI measurements recently reported by Markl et al. (15). The results also suggest that higher spatial resolution is needed for accurately estimating OSI in some of the voxels. Notably, voxel (h) presents both positive and negative velocity components simultaneously during postsystolic deceleration. This indicates that the spatial resolution was insufficient, and the assumption of a monotonically decreasing velocity profile within the voxel was violated.

DISCUSSION

The peak systolic WSR values measured in vivo with the proposed method are higher than those typically reported in the literature for the common carotid arteries (11,13–16,20,22) but within the range of normal values in healthy individuals (1,3,21,28–31). Reported ranges of carotid WSR and WSS values in healthy volunteers vary significantly across the literature, in particular when comparing different techniques (11). CFD simulations are sensitive to many assumptions and simplifications regarding wall compliance, boundary conditions, and properties of blood and endothelium. Techniques for noninvasive in vivo assessment of WSS reported in the literature typically measure the shear rate at some distance from the wall, where the shear rate is lower than at the wall, and then use some kind of assumption about the shape of the velocity profile (e.g., parabolic flow) in order to extrapolate the true wall shear (9). However, peak systolic flow is often not fully developed and hence does not have a parabolic profile (13).

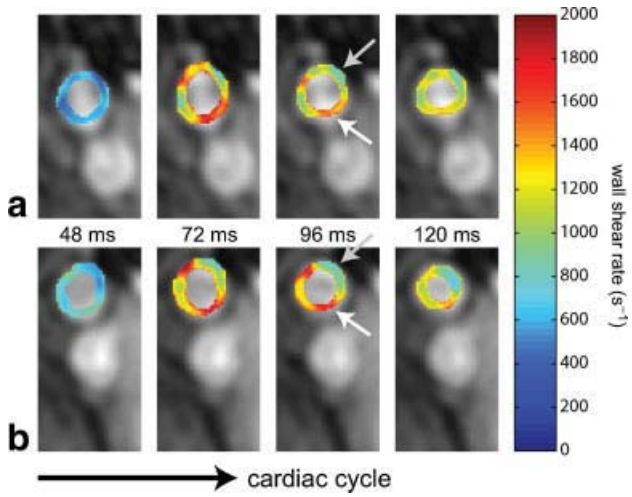

FIG. 8. Repeatability evaluation of the proposed method: **(a)** first study; **(b)** second study (2 weeks later). Regions of low and high WSR match reasonably well in the two studies (arrows). Results correspond to the cardiac phases acquired 48–120 ms after the ECG trigger and to a slice prescribed 5 mm below the carotid bifurcation of subject #3. [Color figure can be viewed in the online issue, which is available at www.interscience.wiley.com.]

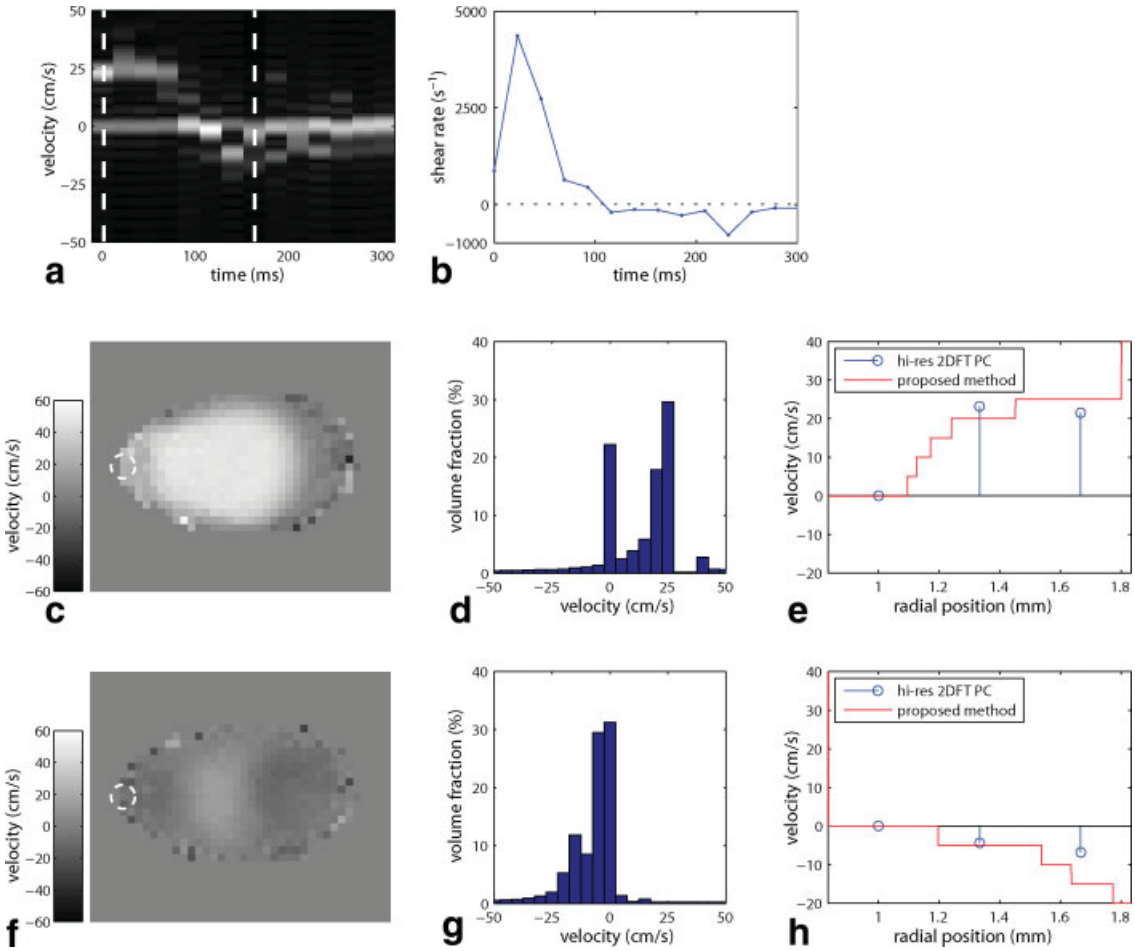

FIG. 9. Oscillatory shear index estimation (proof of concept). A simulated spiral FVE time-velocity distribution—derived from high resolution 2DFT PC data—was obtained for a voxel from a cross-sectional slice at the bifurcation of a pulsatile carotid flow phantom **(a)**. The WSR was estimated for each temporal frame using the proposed method **(b)**. The process is illustrated for the temporal frames at 0 ms **(c–e)** and 162 ms **(f–h)**. The voxel's instantaneous FVE velocity distribution **(d,g)** is obtained from the PC velocity map **(c,f)** using Eq. 2 (the voxel of interest is circled). The intravoxel velocity profile is estimated from the FVE distribution using Eq. 4 and compared with the PC velocity profile **(e,h)**. The OSI for this voxel was estimated to be 0.19. [Color figure can be viewed in the online issue, which is available at www.interscience.wiley.com.]

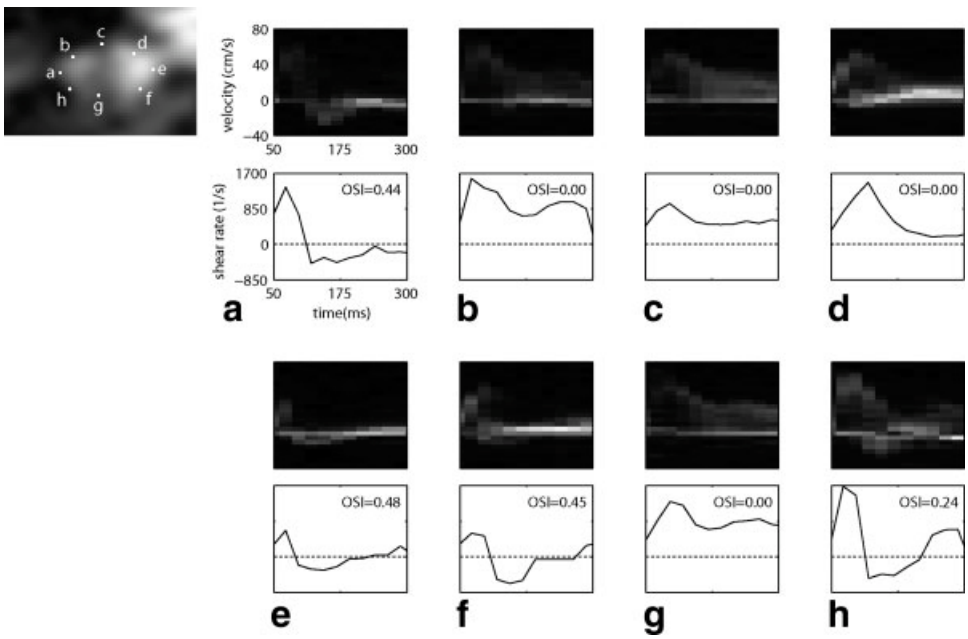

FIG. 10. In vivo assessment of OSI. Results are shown for eight representative voxels **(a–h)**, selected around the circumference of the wall of the carotid bifurcation of subject #3 (see inset). Measured velocity distributions, WSRs, and OSI values, corresponding to the systolic portion of the cardiac cycle, are shown for each voxel.

The use of such assumption for calculation of peak WSS may result in underestimation of peak WSS (9). Furthermore, methods that use spatial resolution of 0.4 mm or coarser will sample only a couple of points along the portion of interest of the velocity profile (viscous sublayer), which is generally not sufficient for reliably extrapolating the velocity profile. Considerably higher spatial resolution would be needed for reliable measurement of WSR in such conditions. The proposed approach allows measuring the shear rate very close to the wall and with very fine spatial resolution and thus eliminates the need for profile extrapolation and of assumption about a parabolic profile. The simulation results presented in Fig. 4 suggest that this technique is capable of estimating WSR values in the carotid arteries with high precision. Nevertheless, the in vivo demonstrations presented in this work should be regarded as feasibility studies, and further validation is needed in order to evaluate the accuracy of the proposed method.

The acquisition and reconstruction parameters used in this work—spatial and velocity resolution values, noise threshold level, and $[v_0,v_1]$ interval range—were selected heuristically and were not optimized. The optimal set of parameters is likely to be subject dependent and spatially and temporally varying. For example, the optimal $[v_0,v_1]$ interval in a region of low wall shear would probably be different from that in a region of high shear. Similarly, the optimal interval at peak flow would probably not be optimal in a cardiac phase with lower peak velocity. In practice, spiral FVE data should be acquired with spatial and velocity resolutions as high as SNR and scan time permit. A fixed threshold value and $[v_0,v_1]$ interval may be useful for an initial assessment, and these may then be manually adjusted for select voxels of interest. This manual assessment may be performed in four quick steps: (i) a flow velocity curve is displayed, and the operator clicks on the cardiac phase of interest; (ii) the WSR map and/or the velocity map of each slice is displayed for the selected cardiac phase, and the operator clicks on the voxel of interest; (iii) the voxel's velocity distribution is displayed, and the operator specifies the noise threshold level; and (iv) the intravoxel velocity profile is displayed, and the operator clicks on the v_0 and v_1 points. These are chosen such that the velocity profile is approximately linear within the specified interval. The v_0 point should be selected as close to zero as possible because we wish to estimate dv/dr at the blood-wall interface. However, we do not recommend using $v_0 = 0$ because the $v = 0$ bin corresponds to static material. The region of the estimated velocity profile corresponding to the viscous sublayer begins at $v = \Delta v$. The voxel's WSR is estimated using linear regression within the specified velocity interval. Alternatively, higher-order polynomials (e.g., quadratic) may be used (9). This could potentially allow the use of broader intervals and reduce the need for operator interaction. Automating parameter selection for reducing operator interaction is a natural continuation of this study and remains as future work. In this feasibility evaluation, operator-guided linear regression was used.

It is desirable to use the thinnest possible slice, as limited by SNR, because variations in WSR may exist along the *z*-axis, notably at the carotid bifurcation. Additionally, the scan plane should be made perpendicular to the vessel wall where WSR is to be estimated because only through-plane velocities are measured. If the scan plane is slightly oblique to the wall, it should be possible to correct both *dv* and *dr* estimates, as long as the carotid geometry relative to the imaged plane is known. Spatial blurring may occur if in-plane velocities are present in the voxels of interest, which would be the case for oblique planes. However, spiral trajectories have been shown to provide excellent immunity to flow artifacts compared with other *k*-space trajectories (e.g., 2DFT, echo-planar imaging), and distortion should be minimal even in the presence of high velocity flow (e.g., stenosis) (32). Spatial blurring due to in-plane flow could potentially be incorporated into the model proposed in Eq. 2, using the formalism introduced by Nishimura et al. (32).

Another potential source of error is spatial blurring due to off-resonance. In order to address this issue, we performed localized gradient shimming and reduced the required readout duration by using variable-density spiral acquisitions (33). Other possible solutions to this problem are presented by Carvalho and Nayak (25). Aliasing artifacts due to variable-density sampling may reduce the accuracy in estimating the position of the wall-blood interface within the voxel, but we did not observe any visible artifacts within the region of interest (the carotid arteries) because a well-localized carotid coil was used.

Other possible sources of error associated with the Frayne method, not related to the use of spiral readouts, are discussed by Frayne and Rutt (23). These include imprecisions associated with measuring the shear rate *near* but not *at* the wall (i.e., the choice of the $[v_0,v_1]$ interval), signal loss at the blood-wall interface due to susceptibility effects caused by local magnetic field inhomogeneity, and ringing and leakage along the velocity dimension due to finite velocity resolution. Although not discussed by Frayne and Rutt (23), finite spatial resolution is also a potential source of error. By "rule of thumb," the voxel should be small enough that at least one third of its volume corresponds to the viscous sublayer. The voxel should also be small enough that the assumption of a monotonically increasing or decreasing intravoxel velocity profile is not violated. These assumptions must be reevaluated when studying subjects with highly stenotic arteries (34–38). It is straightforward to determine if one of these conditions has been violated by analyzing the velocity distributions. For example, if the velocity distribution within a voxel contains both positive and negative velocity components simultaneously, then the second condition has not been met, and higher resolution must be used. Another potential problem associated with finite spatial resolution is that truncation in *k*-space results in blurring, which can be modeled as a convolution of the object with a kernel, consisting of a main lobe and side lobes. The side lobes cause crosstalk between neighboring voxels, while the main lobe causes intravoxel weighting. The side lobes may be reduced by windowing the *k*-space data; however, this process reduces the effective spatial resolution and increases the intravoxel weighting effect.

Voxel shape is also a potential source of error. Frayne and Rutt (23) assume that voxels are squares and that the radial velocity gradient is along one of the voxel axes (which is generally not true). In spiral FVE, the voxel shape is circular; therefore, no assumption needs to be made about

the direction of the velocity gradient. However, the volume fraction corresponding to each velocity bin is no longer directly proportional to its associated radial distance. In a circular voxel, the relationship between volume fraction and radial distance varies with intravoxel position. With full knowledge of the voxel shape (including k-space truncation and potentially off-resonance), voxel shape and intravoxel weighting effects may be compensated by "equalizing" the velocity histogram before reconstructing the velocity profile.

Acceleration is not expected to cause WSR estimation errors. Acceleration in FVE imaging results in a linear phase along k_v, i.e., a shift of the velocity distribution along v (39). Assuming constant acceleration (a) between excitation and readout, the phase accrual at echo time is $\phi = 2\pi k_v v + 2\pi k_a a$, where $k_v = \gamma M_1$ and $k_a = \gamma M_2/2 = \frac{M_2/2}{M_1} k_v$, where γ is the gyromagnetic, and M_1 and M_2 are the first and second moments of the z gradient, respectively. If $a = 0$, then $\phi = 2\pi k_v v$, as expected. For $a \neq 0$, $\phi = 2\pi k_v(v + \frac{M_2/2}{M_1} a)$. Hence, the measured $s(v)$ will be shifted by $\frac{M_2/2}{M_1} a$. The same effect is observed in PC imaging. The $\frac{M_2/2}{M_1}$ ratio for the gradients used in our in vivo experiment is 3 ms. Typical peak blood acceleration values in the common carotid arteries of healthy individuals are on the order of 500 cm/sec^2 (40). Therefore, the maximum expected shift is less than 2 cm/sec, while the velocity resolution is 5 cm/sec, and typical peak velocities in normals are on the order of 70 cm/sec (less than 3% error). Furthermore, the Frayne method is insensitive to shifts in the velocity profile, as long the $[v_0, v_1]$ interval is adjusted accordingly.

Due to its high dimensionality (x, y, z, v, t), spiral FVE has great potential for high orders of acceleration (41). Several approaches have been proposed to drastically reduce the acquisition time of FVE imaging without significant loss of information (41–46). Furthermore, if the subject's head and neck can be successfully immobilized and hemodynamic conditions are relatively stable, higher acceleration could be achieved by using three-dimensional imaging (a stack of spirals in k_x, k_y, k_z) (47) instead of multiple two-dimensional acquisitions. This would not only increase SNR and allow for higher orders of parallel imaging acceleration (48,49) but also allow even higher factors of temporal (50) and compressed-sensing-based (51) acceleration.

CONCLUSIONS

We have demonstrated a method for noninvasive in vivo assessment of carotid WSR in clinically feasible scan times. Spiral FVE acquisitions were used with the wall shear rate computation method proposed by Frayne and Rutt (23). The achieved temporal resolution was sufficient to capture the oscillatory pattern of carotid WSR, a potentially important factor involved in atherosclerotic plaque accumulation. We have shown that velocity distributions measured with spiral FVE agree well with those obtained with 2DFT PC, the current MR gold standard. In the process, we described a model for deriving FVE data from high-resolution velocity maps, which can be used for many simulation purposes. We used this model to demonstrate that the spiral FVE/Frayne method accurately estimates carotid WSR from simulated data obtained using CFD and to demonstrate the feasibility of OSI estimation using the proposed method.

Spiral FVE is uniquely suitable for in vivo WSR estimation as it is the only currently available FVE method capable of providing fully-resolved spatial localization in clinically practical scan time. The acquisition time of the proposed method can be drastically reduced using established and emerging acceleration techniques, due to the high dimensionality of the spiral FVE data. The proposed spiral FVE/Frayne method may facilitate our understanding of the relationship between hemodynamics and the process of atherosclerotic plaque formation, growth, and rupture.

ACKNOWLEDGMENTS

The authors thank Lisong Ai and Tzung Hsiai for providing the CFD velocity maps used in this work, Thomas and Barbara Burke (Phantoms by Design Inc., Bothell, WA) and Kyunghyun Sung for their support and collaboration, and Ajit Yoganathan, Kartik Sundareswaran, John Oshinski, and Fernando Salvucci for useful discussions. This work was supported by a fellowship from the Graduate School of the University of Southern California (to J.L.A.C.).

REFERENCES

1. Zarins CK, Giddens DP, Bharadvaj BK, Sottiurai VS, Mabon RF, Glagov S. Carotid bifurcation atherosclerosis: quantitative correlation of plaque localization with flow velocity profiles and wall shear stress. Circ Res 1983;53:502–514.
2. Tang D, Yang C, Mondal S, Liu F, Canton G, Hatsukami T, Yuan C. A negative correlation between human carotid atherosclerotic plaque progression and plaque wall stress: in vivo MRI-based 2D/3D FSI models. J Biomech 2008;41:727–736.
3. Ku DN, Giddens DP, Zarins CK, Glagov S. Pulsatile flow and atherosclerosis in the human carotid bifurcation: positive correlation between plaque location and low oscillating shear stress. Arterioscler Thromb Vasc Biol 1985;5:293–302.
4. Dai G, Kaazempur-Mofrad MR, Natarajan S, Zhang Y, Vaughn S, Blackman BR, Kamm RD, Garcia-Cardena G, Gimbrone MA Jr. Distinct endothelial phenotypes evoked by arterial waveforms derived from atherosclerosis-susceptible and -resistant regions of human vasculature. Proc Natl Acad Sci USA 2004;101:14871–14876.
5. Thubrikar MJ, Robicsek F. Pressure-induced arterial wall stress and atherosclerosis. Ann Thorac Surg 1995;59:1594–1603.
6. Adamson SL, Roach MR. Measurement of wall shear stress in a glass renal bifurcation technique that monitors the erosion of an opaque coating layer. Biorheology 1981;18:9–21.
7. Ling SC, Atabek HB, Fry DL, Patel DJ, Janicki JS. Application of heated-film velocity and shear probes to hemodynamic studies. Circ Res 1968;23:789–801.
8. Hsiai TK, Cho SK, Wong PK, Ing MH, Salazar A, Hama S, Navab M, Demer LL, Ho CM. Micro sensors: linking inflammatory responses with oscillatory shear stress. Ann Biomed Eng 2004;32:189–201.
9. Lou Z, Yang WJ, Stein PD. Errors in the estimation of arterial wall shear rates that result from curve fitting of velocity profiles. J Biomech 1993;26:383–390.
10. Brands PJ, Hoeks AP, Hofstra L, Reneman RS. A noninvasive method to estimate wall shear rate using ultrasound. Ultrasound Med Biol 1995;21:171–185.
11. Barker AJ, Zhang F, Gates PE, Mazzaro LA, Fulford J, Lanning CJ, Shandas R. Wall shear stress measurement error in the common carotid artery: a dual modality study. In: Proc, International Society for Magnetic Resonance in Medicine, 17th Annual Meeting, Honolulu, 2009. p 3784.
12. Stokholm R, Oyre S, Ringgaard S, Flaagoy H, Paaske WP, Pedersen EM. Determination of wall shear rate in the human carotid artery by magnetic resonance techniques. Eur J Vasc Endovasc Surg 2000;20:427–433.

13. Oshinski JN, Curtin JL, Loth F. Mean-average wall shear stress measurements in the common carotid artery. J Cardiovasc Magn Reson 2006;8:717–722.
14. Sui B, Gao P, Lin Y, Gao B, Liu L, An J. Assessment of wall shear stress in the common carotid artery of healthy subjects using 3.0-tesla magnetic resonance. Acta Radiol 2008; 49:442–449.
15. Markl M, Wegent F, Bauer S, Stalder AF, Frydrychowicz A, Weiller C, Schumacher M, Harloff A. Three-dimensional assessment of wall shear stress distribution in the carotid bifurcation. In: Proc, International Society for Magnetic Resonance in Medicine, 17th Annual Meeting, Honolulu, 2009. p 323.
16. Duivenvoorden R, de Groot E, van Bavel E, Amri R, Stroes E, Lameris J, Kastelein J, Nederveen AJ. 3.0 Tesla MRI common carotid wall shear stress measurements: correlations with common carotid arterial wall thickness. In: Proc, International Society for Magnetic Resonance in Medicine, 17th Annual Meeting, Honolulu, 2009. p 1842.
17. Tang C, Blatter DD, Parker DL. Accuracy of phase-contrast flow measurements in the presence of partial-volume effects. J Magn Reson Imaging 1993;3:377–385.
18. Boussel L, Rayz V, Martin A, Acevedo-Bolton G, Lawton MT, Higashida R, Smith WS, Young WL, Saloner D. Phase-contrast magnetic resonance imaging measurements in intracranial aneurysms in vivo of flow patterns, velocity fields, and wall shear stress: comparison with computational fluid dynamics. Magn Reson Med 2009;61: 409–417.
19. Harloff A, Albrecht F, Spreer J, Stalder AF, Bock J, Frydrychowicz A, Schollhorn J, Hetzel A, Schumacher M, Hennig J, Markl M. 3D blood flow characteristics in the carotid artery bifurcation assessed by flow-sensitive 4D MRI at 3T. Magn Reson Med 2009;61:65–74.
20. Steinman DA, Thomas JB, Ladak HM, Milner JS, Rutt BK, Spence JD. Reconstruction of carotid bifurcation hemodynamics and wall thickness using computational fluid dynamics and MRI. Magn Reson Med 2002;47:149–159.
21. Papathanasopoulou P, Zhao S, Köhler U, Robertson MB, Long Q, Hoskins P, Xu XY, Marshall I. MRI measurement of time-resolved wall shear stress vectors in a carotid bifurcation model, and comparison with CFD predictions. J Magn Reson Imaging 2003;17:153–162.
22. Kim CS, Kiris C, Kwak D, David T. Numerical simulation of local blood flow in the carotid and cerebral arteries under altered gravity. J Biomed Eng 2006;128:194–202.
23. Frayne R, Rutt BK. Measurement of fluid-shear rate by Fourier-encoded velocity imaging. Magn Reson Med 1995;34:378–387.
24. Moran PR. A flow velocity zeugmatographic interlace for NMR imaging in humans. Magn Reson Imaging 1982;1:197–203.
25. Carvalho JLA, Nayak KS. Rapid quantitation of cardiovascular flow using slice-selective Fourier velocity encoding with spiral readouts. Magn Reson Med 2007;57:639–646.
26. Ai L, Rouhanizadeh M, Wu JC, Takabe W, Yu H, Alavi M, Li R, Chu Y, Miller J, Heistad DD, Hsiai TK. Shear stress influences spatial variations in vascular Mn-SOD expression: implication for LDL nitration. Am J Physiol Cell Physiol 2008;294:1576–1585.
27. He X, Ku DN. Pulsatile flow in the human left coronary artery bifurcation: average conditions. J Biomech Eng 1996;118:74–82.
28. Samijo SK, Willigers JM, Barkhuysen R, Kitslaar PJEHM, Reneman RS, Brands PJ, Hoeks APG. Wall shear stress in the human common carotid artery as function of age and gender. Cardiovasc Res 1998;39:515–522.
29. Malek AM, Alper SL, Izumo S. Hemodynamic shear stress and its role in atherosclerosis. JAMA 1999;282:2035–2042.
30. Ding Z, Wang K, Li J, Cong X. Flow field and oscillatory shear stress in a tuning-fork-shaped model of the average human carotid bifurcation. J Biomech 2001;34:1555–1562.
31. Reneman RS, Arts T, Hoeks APG. Wall shear stress—an important determinant of endothelial cell function and structure—in the arterial system in vivo: discrepancies with theory. J Vasc Res 2006;43: 251–269.
32. Nishimura DG, Irarrazabal P, Meyer CH. A velocity k-space analysis of flow effects in echo-planar and spiral imaging. Magn Reson Med 1995;33:549–556.
33. Tsai CM, Nishimura DG. Reduced aliasing artifacts using variable-density k-space sampling trajectories. Magn Reson Med 2000;43: 452–458.
34. Ghalichi F, Deng X, De Champlain A, Douville Y, King M, Guidoin R. Low Reynolds number turbulence modeling of blood flow in arterial stenoses. Biorheology 1998;35:281–294.
35. Stroud JS, Berger SA, Saloner D. Numerical analysis of flow through a severely stenotic carotid artery bifurcation. J Biomech Eng 2002;124: 9–20.
36. Ghalichi F, Deng X. Turbulence detection in a stenosed artery bifurcation by numerical simulation of pulsatile blood flow using the low-Reynolds number turbulence model. Biorheology 2003;40:637–654.
37. Tortoli P, Michelassi V, Bambi G, Guidi F, Righi D. Interaction between secondary velocities, flow pulsation and vessel morphology in the common carotid artery. Ultrasound Med Biol 2003;29:407–415.
38. Younis BA, Berger SA. A turbulence model for pulsatile arterial flows. J Biomech Eng 2004;126:578–584.
39. Nayler GL, Firmin DN, Longmore DB. Blood flow imaging by cine magnetic resonance. J Comput Assist Tomogr 1986;10:715–722.
40. Chemla D, Demolis P, Thyrault M, Annane D, Lecarpentier Y, Giudicelli JF. Blood flow acceleration in the carotid and brachial arteries of healthy volunteers: respective contributions of cardiac performance and local resistance. Fundam Clin Pharmacol 1996;10:393–399.
41. Carvalho JLA, Nayak KS. Accelerated spiral Fourier velocity encoded imaging. In: Proc, International Society for Magnetic Resonance in Medicine, 15th Annual Meeting, Berlin, 2007. p 588.
42. Hansen MS, Baltes C, Tsao J, Kozerke S, Pruessmann KP, Boesiger P, Pedersen EM. Accelerated dynamic Fourier velocity encoding by exploiting velocity-spatio-temporal correlations. MAGMA 2004;17:86–94.
43. DiCarlo JC, Hargreaves BA, Nayak KS, Hu BS, Pauly JM, Nishimura DG. Variable-density one-shot Fourier velocity encoding. Magn Reson Med 2005;54:645–655.
44. Macgowan CK, Madore B. Application of UNFOLD to real-time Fourier velocity encoding. In: Proc, International Society for Magnetic Resonance in Medicine, 14th Annual Meeting, Seattle, 2006. p 872.
45. Carvalho JLA, DiCarlo JC, Kerr AB, Nayak KS. Reconstruction of variable-density data in Fourier velocity encoding. In: Proc, International Society for Magnetic Resonance in Medicine, 15th Annual Meeting, Berlin, 2007. p 2514.
46. Gamper U, Boesiger P, Kozerke S. Compressed sensing in dynamic MRI. Magn Reson Med 2008;59:365–373.
47. Irarrazabal P, Nishimura DG. Fast three-dimensional magnetic resonance imaging. Magn Reson Med 1995;33:656–662.
48. Weiger M, Pruessmann KP, Boesiger P. 2D SENSE for faster 3D MRI. MAGMA 2002;14:10–19.
49. Blaimer M, Breuer FA, Mueller M, Seiberlich N, Ebel D, Heidemann RM, Griswold MA, Jakob PM. 2D-GRAPPA-operator for faster 3D parallel MRI. Magn Reson Med 2006;56:1359–1364.
50. Kozerke S, Tsao J, Razavi R, Boesiger P. Accelerating cardiac cine 3D imaging using k-t BLAST. Magn Reson Med 2004;52:19–26.
51. Lustig M, Donoho DL, Pauly JM. Sparse MRI: the application of compressed sensing for rapid MR imaging. Magn Reson Med 2007;58:1182–1195.